

A New Tightly-Coupled Dual-VIO for a Mobile Manipulator with Dynamic Locomotion

Jianxiang Xu and Soo Jeon

Abstract—This paper introduces a new dual monocular visual-inertial odometry (dual-VIO) strategy for a mobile manipulator operating under dynamic locomotion, i.e. coordinated movement involving both the base platform and the manipulator arm. Our approach has been motivated by challenges arising from inaccurate estimation due to coupled excitation when the mobile manipulator is engaged in dynamic locomotion in cluttered environments. The technique maintains two independent monocular VIO modules, with one at the mobile base and the other at the end-effector (EE), which are tightly coupled at the low level of the factor graph. The proposed method treats each monocular VIO with respect to each other as a positional anchor through arm-kinematics. These anchor points provide a soft geometric constraint during the VIO pose optimization. This allows us to stabilize both estimators in case of instability of one estimator in highly dynamic locomotions. The performance of our approach has been demonstrated through extensive experimental testing with a mobile manipulator tested in comparison to running dual VINS-Mono in parallel. We envision that our method can also provide a foundation towards active-SLAM (ASLAM) with a new perspective on multi-VIO fusion and system redundancy.

Index Terms—mobile manipulator, visual-inertial odometry, dynamic locomotion, sensor fusion

I. INTRODUCTION

MOBILE robots have been increasingly adopted in warehouses, while the manipulator arm has long operated in many manufacturing plants. A mobile manipulator, a combination of both, has become an attractive candidate for various tasks requiring dynamic movement and dexterous manipulation [1].

Historically, the mobile robot navigation problem comprises three sub-problems; mapping, localization, and motion planning [2]. The first two problems are combined in the context of simultaneous localization and mapping (SLAM), proposed by Smith et al. in 1986 [3].

As the interest in this field grows, SLAM has progressed in various forms with different sensors (inertial measurement unit (IMU), light detection and ranging (LIDAR), time-of-flight (ToF), encoders and vision) with various fusion approaches (filtering or graph optimization) [4]. In particular, visual-SLAM (VSLAM) has been popular in recent years due to its low cost and rich perception [5]. Often, VSLAM and visual odometry (VO) are used interchangeably in the literature with slightly different objectives; the former focuses on the global and consistent estimate of a device's path, while the latter emphasizes the real-time pose estimations [4]. One may regard

the VO with loop-closure as a complete SLAM. To enhance the robustness and performance of SLAM, high rate IMU data have been incorporated to realize visual-inertial-SLAM (VISLAM) and visual inertial odometry (VIO), which was used for a tightly-coupled fusion with vision in multi-state constraint Kalman filter (MSCKF) [6].

As the SLAM becomes more mature, a new frontier work in active-SLAM (ASLAM) has gained attention, aiming to unify all three sub-problems of navigation by bringing the task of actively planning robot locomotion to balance between exploitation (to decrease pose uncertainty) and exploration (to increase the map coverage) [2], [7].

A mobile manipulator can be a great platform to adopt ASLAM with additional sensor at the end-effector (EE) of the manipulator. However, many SLAM modules of mobile manipulators rely solely on the base platform aided by other costly sensors such as LIDAR [8]. Some use EE localization with markers (e.g. ArUco Markers) [9], [10] which are often unusable in a rapidly changing unknown environment with dynamic locomotion [1], [9]. Manipulator arms provide greater spatial flexibility and precise kinematic information through high-resolution encoders. However, due to transmission gaps and mechanical vibration, the EE may run into uncontrollable instability in global poses [11]. As a result, the manipulator can be in an uncertain state of kinematics and dynamics [10], [12], especially in the vicinity of singularity. Consequently, the nominal calibration of IMU noise is practically unsuitable for VIO systems when the EE is in dynamic motion.

Many mobile platforms use omnidirectional wheels to enable agile and holonomic movements. However, the performance of dead-reckoning estimates can be poor due to wheel slippage [1], [13]. These wheels are not ideal for VIO, because excitations from uneven terrains can make the odometry diverge, especially when the field of view (FOV) is limited and features are poorly extracted with frequent occlusions [14]. Moreover, the initialization of VIO may become degenerative for some planar motions, resulting in inaccurate or unobservable spatiotemporal calibration [15], [16]. In fact, for VINS-Mono [17], these motions can be problematic for its initial structure from motion (SfM), causing a delayed initialization.

Mobile manipulators are frequently equipped with an additional camera with IMU near the wrist or the EE (a.k.a. the eye-in-hand vision) for perception and manipulation. This makes two VIOs readily available from the system, one at the mobile base and the other near the EE. Combining these two sensory modules offers great flexibility when one sensor is unreliable or unavailable. However, the increased degree-of-freedom (DOF) comes at a price: increased system uncertain-

The authors are with the Department of Mechanical and Mechatronics Engineering, University of Waterloo, Waterloo, Canada (email: jack.xu@uwaterloo.ca, soojeon@uwaterloo.ca)

ties due to coupled excitation when engaged in dynamic movement on different unknown terrains [1], [18]. This results in highly non-uniform pose uncertainties for both VIO modules. Current SLAM systems often fail when the robot's motion is too complex or the environment is too challenging, e.g. highly dynamic locomotion in cluttered environments [19].

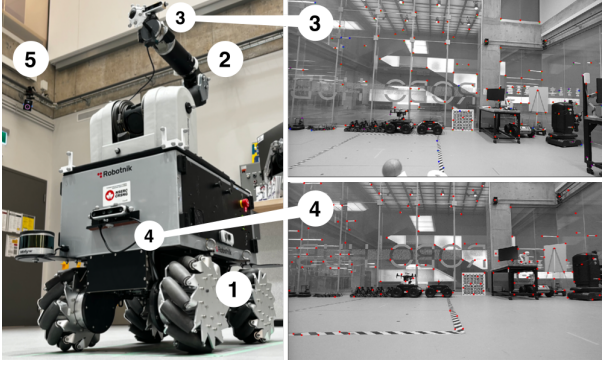


Fig. 1. Our mobile manipulator comprises a 3-DOF SUMMIT mobile base ① and a 7-DOF WAM robotic arm ②. It has two D455 cameras configured with only monocular-RGB and IMU; one located at the EE ③ and the other at the base ④. A Vicon system ⑤ is used for ground truth (GT).

This motivates us to develop a more robust low-cost real-time dual-VIO system for a mobile manipulator with dynamic locomotion. In this paper, dynamic locomotion refers to coordinated movement involving both the base platform and the manipulator arm. Figure 1 depicts a basic setup for our study, which employs one set of a monocular camera with an IMU installed on the holonomic mobile base (3-DOF SUMMIT XL from Robotnik Inc.) and another set at the EE of the manipulator (7-DOF WAM Arm from Barrett Inc.).

To the authors' best knowledge, this is the first paper introducing a tightly-coupled dynamic dual monocular VIOs on a mobile manipulator by combining proprioception (VIO) and kinesthesia (arm odometry) at the low level of the factor graph. Our key contributions are two-fold;

- Construction of a new tightly coupled dual-VIO approach that balances robustness and computational complexity by incorporating the arm odometry factor.
- Implementation of a modular distributed dual-VIO architecture that can be applied to general configurations of mobile manipulator platforms such as the one with multiple manipulators or a legged robot with a manipulator.

II. RELATED WORKS

A. Visual Inertial Odometry (VIO)

VIO is often divided into stereo-VIO and monocular VIO. We are interested in monocular VIO due to its simplicity and low cost without losing richness in information [5]. The stereo-VIO allows better 3D reconstruction but requires much higher data bandwidth. Since the monocular VIO relies on the triangulation between consecutive-frame features (as opposed to calibrated stereo triangulation), it is more prone to translational errors in the pose estimation [20].

Similar to most of SLAM algorithms, VIO consists of two main concurrent components:

1) *Front-end*: The front-end module handles feature tracking and data extraction, which can be either sparse (feature) or dense (direct). The sparse methods have been predominant due to its robustness and efficiency. The performance of the front-end has a direct impact on the accuracy of the back-end [21]. Hence, many works focused on improving the front-end with additional features (e.g. point and line features [22], shape features [23]), or image enhancements [24].

2) *Back-end*: The back-end module is often associated with sensor fusion. It may be categorized into either filter-based or graph-based. Filter-based methods rely on the principle of Bayes filters as their foundational form with certain relaxation [25], such as Gaussian approximation with extended Kalman filter (EKF) (e.g. MSCKF [6]). Meanwhile, most graph-based methods (a.k.a. optimization-based) are derived from Bayesian inference and draw on recent advances in non-linear optimization solvers (e.g. Ceres [26] used in VINS-Mono [17]). When we assume simple linear Gaussian additive noise, maximum-a-posteriori (MAP) inference becomes equivalent to Kalman smoothing, and the tracking problem leads to the Kalman filter (KF) [27]. In practice, the filtering is preferred for high-rate and locally consistent data (IMU), while graph-based techniques are more efficient with low-rate, globally consistent, sparse features (images).

B. VIO Fusion on Different Platforms

Modelling errors, sensor noise, feature mis-identification, and external disturbances are inevitable, hindering accurate estimation and introducing drifts [28]. To address these issues, VIO is frequently integrated with other sensors (e.g. global positioning system (GPS) or encoders) tailored towards a specific platform (e.g. aerial, legged, or mobile manipulator) for different environments (e.g. indoor or outdoor). For instance, unmanned aerial vehicles (UAVs) often require additional fixed positioning systems to provide low-rate correction. In outdoors, global navigation satellite system (GNSS) is commonly combined with VIO through optimization (e.g. [15], [29]) or filtering (e.g. [30] based on MSCKF). Similarly, ultra wide-band (UWB) data can be fused with VIO (e.g. [31]) in indoors. However, fixed positioning systems are often unavailable in cluttered and unknown environments where mobile and legged robots operate. Instead, dead reckoning sensors are used with VIO. Vehicle encoders are commonly fused tightly into the VIO through the vehicle dynamics model (e.g. [32]) or the kinematics model (e.g. [33]) to improve its robustness.

For legged robots, dynamic locomotion involves more sudden, jerky movements and impacts from ground touchdowns. These movements can significantly disrupt vision sensors, making it challenging for general VIO to estimate the robot's state accurately [34]. Hence, the additional joint encoders can be tightly coupled with VIO in the form of legged odometry factor in the factor graph to minimize the drift [35], [36], [37].

In mobile manipulators, similar challenges arise not only from the ground impacts but also from the dynamic coupling between the base and the arm during the dynamic locomotion. As a result, the base disturbances (from wheel-ground interactions) propagate to the arm vibration, while the arm vibrations

propagate back to the base body [13]. This oscillatory coupling amplifies the disturbance experienced at both the base and the EE VIO modules at certain modes, depending on the arm configuration. To address this challenge, [9] has tried to combine the VIO at the mobile base and that at the EE through moving horizon estimator (MHE) with the help of fiducial markers. The study suggests that the IMU is more effective in measuring the EE when compared to the base. The results also indicate that combining the base camera with the arm odometry helps to calibrate the cameras' position with respect to the manipulator and the joint angle biases.

These findings motivated us to develop a dual-VIO system capable of localizing during dynamic locomotion in an unstructured, marker-free environment. This is achieved by simultaneously maintaining two factor-graph-based VIOs closely interacting with each other through arm kinematics.

C. Multi-VIO Fusion

Depending on the degree or level with which multiple sensors are fused, one may classify a general multi-sensor fusion into two categories;

1) *Loosely-coupled*: The core idea of loosely-coupled fusion is to blend poses from different estimators through a weighted combination. It is a simple and efficient way to unite various sensors and odometry algorithms through a filter-based method, and thus widely used in classical multi-modal fusion (e.g. [38]). [39] showed improved robustness in estimation and faster reconstruction of dense point cloud through a delayed fusion of multiple-VO integrating IMU into an error-state space KF. In fact, the multi-VIO can be considered as an example of mixture of experts (MoE) problem [40]. However, failure of one sensor may cause deterioration or divergence of the whole estimation [41]. In practice, it is not easy to characterize different uncertainties and errors [40].

2) *Tightly-coupled*: Tightly-coupled methods prefer to fuse sensor data locally through a single optimization (e.g. non-overlapping multi-cameras [42], [43], [44]) and solve the pose and position jointly. Often, this approach relies on the flexibility and modularity of graph optimization. It may suffer from computational complexity due to scaling issues; the network keeps growing as more optimization states are introduced [40].

In Multi-VIO Fusion, all methods above improved robustness with faster reconstruction, benefiting from the increased FOV and sensory redundancy. We propose a new technique involving a moderate tight-coupling¹ to balance robustness and computational complexity while maintaining the independence of each VIO for system redundancy and failure recovery.

D. Monocular-VIO and VINS-Mono

We are particularly interested in monocular-VIO due to its simplicity, as discussed in Section I. In particular, VINS-Mono has already demonstrated its robust performance with fewer resources [35], [20], [46] making it the baseline of many relevant works including ours. Readers interested in VINS-Fusion with a monocular setup may refer to the original works [2], [17] for in-depth fundamentals and architecture.

¹In some literature (e.g. [45]), the term "semi-tight-coupling" has been used, but we adopt "tight-coupling" as a more generally accepted term.

III. FORMULATION OF PROPOSED DUAL VIOS

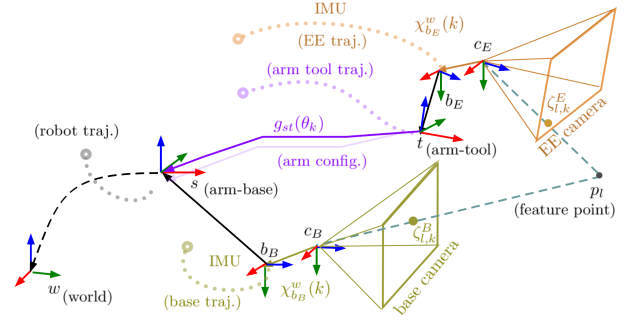


Fig. 2. Frames and their relations: Solid arrows show constrained transformation; dashed arrows show unconstrained transformation; dotted lines show time-varying trajectories with a starting knot. To simplify matters, we assume that the state estimation is performed at the camera's IMU frame for both the base and the EE (i.e. $\chi_{b_B}^w, \chi_{b_E}^w \in \mathbf{SE}(3)$). The kinematic parameters for the arm are calibrated offline based on the Vicon and 3D model at its zero-configuration, where the arm is straightened upwards ($g_{st}(\mathbf{0}) \in \mathbf{SE}(3)$).

The objective of the dual-VIO is to estimate the poses ($\chi \in \mathbf{SE}(3)$) of the camera bodies with respect to their initial poses in the world frame (w) both at the mobile base (b_B) and the EE (b_E), concurrently on the fly throughout locomotion. Figure 2 depicts configuration of coordinate frames used in this paper. For each motion variable (e.g. the $\chi_{b_E}^w$), the superscript denotes its frame of reference while the subscript denotes the frame whose motion is described by the variable. The pose estimate is directly obtained from the state at frame k (denoted by \mathbf{x}_{b_k}), which is to be estimated by the factor graph (See Eq. (2)).

A. Formulation of Factor Graph

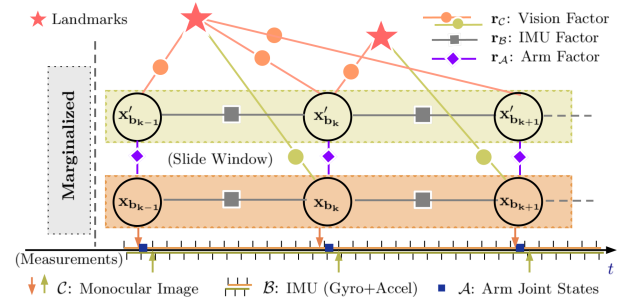


Fig. 3. Illustration of the sliding window dual factor graph structure with the arm odometry factor coupling two states, with \mathbf{x}_{b_k} as the primary state and \mathbf{x}'_{b_k} as the corresponding secondary state at frame k . The bottom timeline shows an approximated representation of measurement timings and sampling strategy; IMU data is sampled and pre-integrated between two frames, images are software synchronized, and arm joint states are sampled at each frame.

The proposed dual-VIO maintains two sets of factor graphs running concurrently in parallel to optimize two independent sets of states, one for the EE and the other for the base (i.e. b_E and b_B , respectively, in Fig. 2). This is distinct from fusing the optimized odometry in a later stage globally (i.e. loosely-coupled fusion) or jointly optimizing both states (i.e. tightly-coupled fusion). Instead, a moderate coupling is introduced through the arm odometry factor from the previously optimized states at the opposing VIO, propagated through the

arm kinematics. This process is depicted in Fig. 3 in the form of primary and secondary VIO. Since either VIO is merely mirroring each other, we will denote \mathbf{x}_{b_k} as the primary VIO state and \mathbf{x}'_{b_k} as the secondary one at the frame k . For instance, from the EE's standpoint, its primary VIO state (i.e. \mathbf{x}_{b_k}) is $\mathbf{x}_{b_E}^w(k)$, while its complementary one (\mathbf{x}'_{b_k}) is $\mathbf{x}_{b_E}^w(k)$. This relative designation also applies to the geometric pose $\chi \in \mathbf{SE}(3)$, i.e. the complementary VIO pose is $\chi'_{b_k} = \chi_{b_E}^w(k)$ if its primary VIO pose is $\chi_{b_k} = \chi_{b_E}^w(k)$.

Let us define $\mathcal{K} := \{0, \dots, n\}$ as the set of integer indices for all the frames from $t_{k=0}$ to $t_{k=n}$ within the horizon. At each frame $k \in \mathcal{K}$ (k is also the discrete-time index for estimation within the horizon), the set of measurements from arm odometry is denoted by $\mathcal{A}_k := \{a_0, \dots, a_n\}$, and that for the IMU is denoted by $\mathcal{Z}_k := \{z_0, \dots, z_n\}$ between two consecutive frames $t \in \{t_k, t_{k+1}\}$. Similarly, \mathcal{C}_k denotes the set of all the image measurements associated with features that had occurred more than once until frame k . We denote $\zeta_{l,j}$ as an element of \mathcal{C}_k , i.e. $\zeta_{l,j} \in \mathcal{C}_k$ ($l \in \{0, \dots, m\}$, $j \in \mathcal{K}$) to associate it explicitly with l -th feature in j -th camera frame that occurs more than once, starting from initial appearance.

Each VIO operates over the optimization variable \mathbf{X} for an independent receding horizon sliding window. Thus, \mathbf{X} contains all state vectors \mathbf{x}_{b_k} 's ($k \in \mathcal{K}$) in the horizon. Besides, it also includes \mathbf{p}_c^b and \mathbf{q}_c^b which denote the relative position and the relative orientation, respectively, between the camera frame and the corresponding body frame. For computational efficiency, \mathbf{X} also contains m inverse feature depth (denoted by λ_i , $i \in \{0, 1, \dots, m\}$) computed from all image measurements \mathcal{C}_k . Namely, the sliding window operates its optimization over

$$\mathbf{X} = [\mathbf{x}_{b_0}, \dots, \mathbf{x}_{b_n}, \mathbf{p}_c^b, \mathbf{q}_c^b, \lambda_0, \dots, \lambda_m] \quad (1)$$

In detail, the state at each frame is a vector

$$\mathbf{x}_{b_k} = \text{col}(\mathbf{p}_{b_k}^w, \mathbf{v}_{b_k}^w, \mathbf{q}_{b_k}^w, \mathbf{b}_a, \mathbf{b}_g), \quad k \in \mathcal{K} \quad (2)$$

where, $\mathbf{p}_{b_k}^w \in \mathbb{R}^3$ denotes position, $\mathbf{v}_{b_k}^w \in \mathbb{R}^3$ is velocity, $\mathbf{q}_{b_k}^w \in \mathbb{Q} \subset \mathbb{R}^4$ is quaternion for orientation, and $\mathbf{b}_a, \mathbf{b}_g \in \mathbb{R}^3$ denote biases of accelerometer and gyroscope, respectively. Note that χ , \mathbf{X} and \mathbf{x} all convey pose information while taking different mathematical forms for different purposes.

The proposed factor graph can be solved by maximizing the posterior estimate of \mathbf{X} using optimization solvers (e.g. the Ceres solver [26]) with the objective function formulated based on bundle adjustment (BA) (similar to [17], [37]) as

$$\min_{\mathbf{X}} \left\{ \left\| \mathbf{r}_p - H_p \mathbf{X} \right\|^2 + \sum_{k \in \mathcal{K}} \sum_{\zeta_{l,j} \in \mathcal{C}_k} \rho \left(\left\| \mathbf{r}_c(\zeta_{l,j}, \mathbf{X}) \right\|_{P_{\zeta_{l,j}}}^2 \right) + \sum_{k \in \mathcal{K}} \left\| \mathbf{r}_z(z_k, \mathbf{X}) \right\|_{P_{z_k}}^2 + \sum_{k \in \mathcal{K}} \left\| \mathbf{r}_A(a_k(\hat{\mathbf{x}}'_k), \mathbf{X}) \right\|_{P_{a_k}}^2 \right\} \quad (3)$$

where \mathbf{r}_p and H_p in the first term come from the marginalization prior. \mathbf{r}_c , \mathbf{r}_z and \mathbf{r}_A denote the residuals for image, IMU, and arm odometry data, respectively. $P_{\zeta_{l,j}}$, P_{z_k} , P_{a_k} are the corresponding covariance matrices used to compute the weighted information matrix for each residual (See [17] for more details). The last term plays a key role in our approach by coupling two VIOs through arm odometry (See Fig. 3), which is explained in more detail below in subsection III-B.

Solving Eq. (3) has $O(n^2)$ space complexity and $O(n^3)$ time complexity with n states in the sliding window. Hence, for M VIO modules in the system, classical tightly coupled VIOs have space and time complexity of $O(M^2 n^2)$ and $O(M^3 n^3)$, respectively. In comparison, the proposed method treats each VIO as a distributed agent coupled through geometric constraints. Thus, the resulting space and time complexity would be $O(Mn^2)$ and $O(Mn^3)$, respectively.

B. Incorporation of Arm Odometry Factor

The arm odometry provides an anchor point to minimize catastrophic excitation from the current VIO without sacrificing significant computing resources. It is computed based on the previously optimized complementary VIO state $\{\hat{\mathbf{x}}'_{b_0}, \dots, \hat{\mathbf{x}}'_{b_n}\}$, where the hat notation is used to denote the solution that achieves the optimization problem (3).

1) *Manipulator Kinematics* : Forward kinematics (FK) of a manipulator maps its N DOF configuration space (which is a subset of $\mathbb{S}^1 \times \dots \times \mathbb{S}^1 \equiv \mathbb{T}^N$, a.k.a. N-Torus) to the EE pose $\chi_t^s \in \mathbf{SE}(3)$. Using the Lie group theory for $\mathbf{SE}(3)$ [47], we can express FK using a twist coordinate $\xi_i \in \mathbb{R}^6$ for each link, which consists of the axis $\omega_i \in \mathbb{R}^3$ and a point $\mathbf{q}_i \in \mathbb{R}^3$ through it. For group operation, ξ_i can be written with the hat notation as $(\xi_i)^\wedge \in \mathfrak{se}(3)$, i.e. Lie algebra of $\mathbf{SE}(3)$;

$$\xi_i = \begin{bmatrix} -\omega_i \times \mathbf{q}_i \\ \omega_i \end{bmatrix} = \begin{bmatrix} \mathbf{v}_i \\ \omega_i \end{bmatrix}, \quad (\xi_i)^\wedge = \begin{bmatrix} \omega_i & \mathbf{v}_i \\ 0 & 0 \end{bmatrix} \quad (4)$$

Accordingly, the FK ($g_{st}(\theta) : \theta \in \mathbb{T}^N \rightarrow \chi_t^s \in \mathbf{SE}(3)$) in Lie group can be defined with the product of exponential formula with each twist $(\xi_i)^\wedge \in \mathfrak{se}(3)$ and corresponding angle $\theta_i \in [0, 2\pi]$, w.r.t. zero configuration $g_{st}(\mathbf{0})$ [47] as

$$g_{st}(\theta) = e^{(\xi_1)^\wedge \theta_1} e^{(\xi_2)^\wedge \theta_2} \dots e^{(\xi_N)^\wedge \theta_N} g_{st}(\mathbf{0}) \quad (5)$$

2) *Arm Odometry* : At every k -th frame for the estimated state $\hat{\mathbf{x}}_{b_k}$, its complementary state $\hat{\mathbf{x}}'_{b_k}$ is firstly contracted onto the pose manifold $\hat{\chi}'_{b_k} \in \mathbf{SE}(3)$. The pose evolves through FK $g_{st}(\theta)$ to the current odometry frame. The resulting estimated pose incorporating arm odometry $\tilde{\chi}_{b_k} \in \mathbf{SE}(3)$ is lastly lifted onto the local parameter space $a_k = (\tilde{\mathbf{p}}_{b_k}, \tilde{\mathbf{q}}_{b_k}) \in \mathbb{R}^3 \times \mathbb{Q}$. The tilde denotes the estimated variable after incorporating arm odometry. Specifically, for the manipulator illustrated in Fig. 2, we can compute the odometry state (i.e. the pose) over $\mathbf{SE}(3)$ for each of the EE and the base VIO's as

$$\begin{aligned} \tilde{\chi}_{b_E}^w(k) &= \hat{\chi}_{b_E}^w(k) T_s^{b_E} g_{st}(\theta) T_{b_E}^t \\ \tilde{\chi}_{b_B}^w(k) &= \hat{\chi}_{b_E}^w(k) T_t^{b_E} g_{st}^{-1}(\theta) T_{b_B}^s \end{aligned} \quad (6)$$

where T_\star^\bullet is the fixed coordinate transform between \bullet and \star .

3) *Residual of Arm Odometry*: The residual is then computed separately in translation and rotation between the current state and the arm odometry state as

$$\mathbf{r}_A(a_k(\hat{\mathbf{x}}'_k), \mathbf{X}) = \begin{bmatrix} \delta \mathbf{p}_k \\ \delta \mathbf{q}_k \end{bmatrix} = \begin{bmatrix} \tilde{\mathbf{p}}_{b_k}^w - \mathbf{p}_{b_k}^w \\ (\mathbf{q}_{b_k}^w)^{-1} \otimes \tilde{\mathbf{q}}_{b_k}^w \end{bmatrix} \quad (7)$$

where \otimes represent quaternion product [48]. The uncertainties at the EE are more prone to disturbances, while the mobile platform is much more stable. Hence, the arm odometry factor

imposes heavier weight for the translation residuals at the EE (with $P_{a_k}^{b_E} = \text{diag}(\frac{1}{250}I_2, \frac{1}{200}, \frac{1}{10}I_4)$ where I_k is a $k \times k$ identity matrix). Conversely, weaker factors are applied in reverse (i.e. those at the base) with $P_{a_k}^{b_B} = \text{diag}(\frac{1}{10}I_2, \frac{1}{20}, \frac{1}{10}I_4)$ to minimize the impact of noise, disturbance, and kinematic modeling uncertainties from the arm. These values for P_{a_k} are manually tuned w.r.t. the image factor $P_{\zeta_{l,j}} = \frac{1}{520}I_2$.

IV. EXPERIMENTS

A. Experiment Setup

The proposed dual-VIO is implemented based on VINS-Fusion under the Robot Operating System (ROS) environment. Two commercially available robotic cameras (D455 from Intel) are configured at the EE and the mobile base as shown in Fig. 1. Each camera is enabled only with one global shutter RGB camera (with a resolution of 1280×720 pixels at 30 [Hz]) and one IMU at 200 [Hz]. Both depth modules are disabled due to their interference with each other and the Vicon system.

The IMU noise parameters were calibrated offline through the Allan Variance (AVAR) [49] based on 5-hour ROS bag files. One collection is performed on a stationary table. Additional characteristics are collected while both cameras are on the powered robot to characterize the combined noise effects from the nominal noise in the system. The on-robot noise parameters are used for the VIO systems.

The intrinsic parameters of each camera are calibrated offline independently with the omnidirectional camera projection model and the radial-tangential distortion model option available through Kalibr toolbox (Kalibr) [50] over a few minutes of the collection. The collection was performed with individual cameras moving around by hand, with the calibration board in view. Next, the camera-IMU extrinsic parameters are calibrated with its stationary IMU parameters.

We performed direct comparisons against the VINS-Fusion through the ablation study of our proposed method to evaluate the effectiveness of our approach. The baseline data is the dual-VIO with two VINS-Fusion concurrently. All other hyperparameters are kept consistent throughout the ablation study.

1) *Environment*: The experiment was conducted under a well-lighted and cluttered indoor facility, which involves repetitive objects, subtle uneven terrain, low-feature ceiling, and reflective glass windows as shown in Fig. 4.

2) *Choreography*: The choreography of the mobile manipulator consists of 35 combinations of locomotion and arm maneuvers involving five arm motions and seven base motions. Figure 5 shows five different arm motions which cover both static and dynamic scenarios, starting from the home position (Fig. 5(a)). Figures 5(b), 5(c), and 5(d) demonstrate a simple strategy of shifting attention to less dynamic regions. Figures 5(e) and 5(f) explore active reconstruction to increase the mapping rate. The seven base maneuvers include three degenerative motions (spinning, forwarding, reversing) and four holonomic movements (triangle, square, circle, and bee-waggle dance). Table I lists each configuration, with v_x and v_y denoting linear speeds, ω_z the angular rate, and t_{base} and t_{EE} as time duration for the base and the EE, respectively.

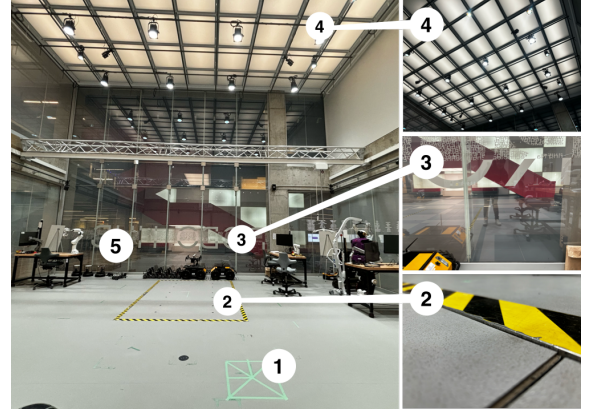


Fig. 4. The environment of a cluttered facility for experiments; ② uneven terrain, ③ reflective glass window, ④ low-feature illuminated ceiling, and ⑤ repetitive robots. The green masking tape (①) on the floor helps operators locate the robot's starting position without collision during the experiment.

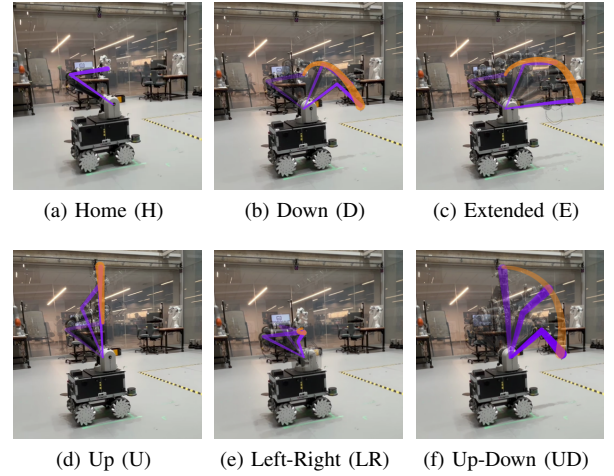


Fig. 5. A collection of six different arm motions with base fixed. (a) showcases the home position of the arm without motion; (b), (c), and (d) demonstrate static arm motion by moving the arm to the desired configuration (i.e. down, forward, up) initially and retracting back to the home (a) at the end of the base movements. (e) and (f) describe dynamic oscillating motions, by sweeping the arm left-and-right and up-and-down, respectively.

TABLE I
CHOREOGRAPHY CONFIGURATION FOR SEVEN BASE MOVEMENTS

		Forward (FWD)	Reverse (RVR)	Spin (SPI)	Triangle (TRI)	Square (SQR)	Circle (SQR)	Bee (BEE)
v_x	m/s	0.2	0.2	0	$\pm 0.3, 0$	0.3, 0	0.3	0.3
v_y	m/s	0	0	0	$\pm 0.3, 0$	$\pm 0.3, 0$	0	0
ω_z	rad/s	0	0	0.2	0	0	0.4	± 0.4
t_{base}	s	20	20	30	30	40	32	50
t_{EE}	s	30	30	40	40	50	42	60

3) *Dataset*: The proposed system is evaluated through the custom dataset collected with our mobile manipulator platform in the 'rosvbag' form. The dataset comprises two sets of monocular cameras and IMU data, which were gathered through six primary arm motions (Fig. 5) and seven basic base motions (Table I). The dataset also includes Vicon data, which serves as ground truth (as illustrated in Fig. 1).

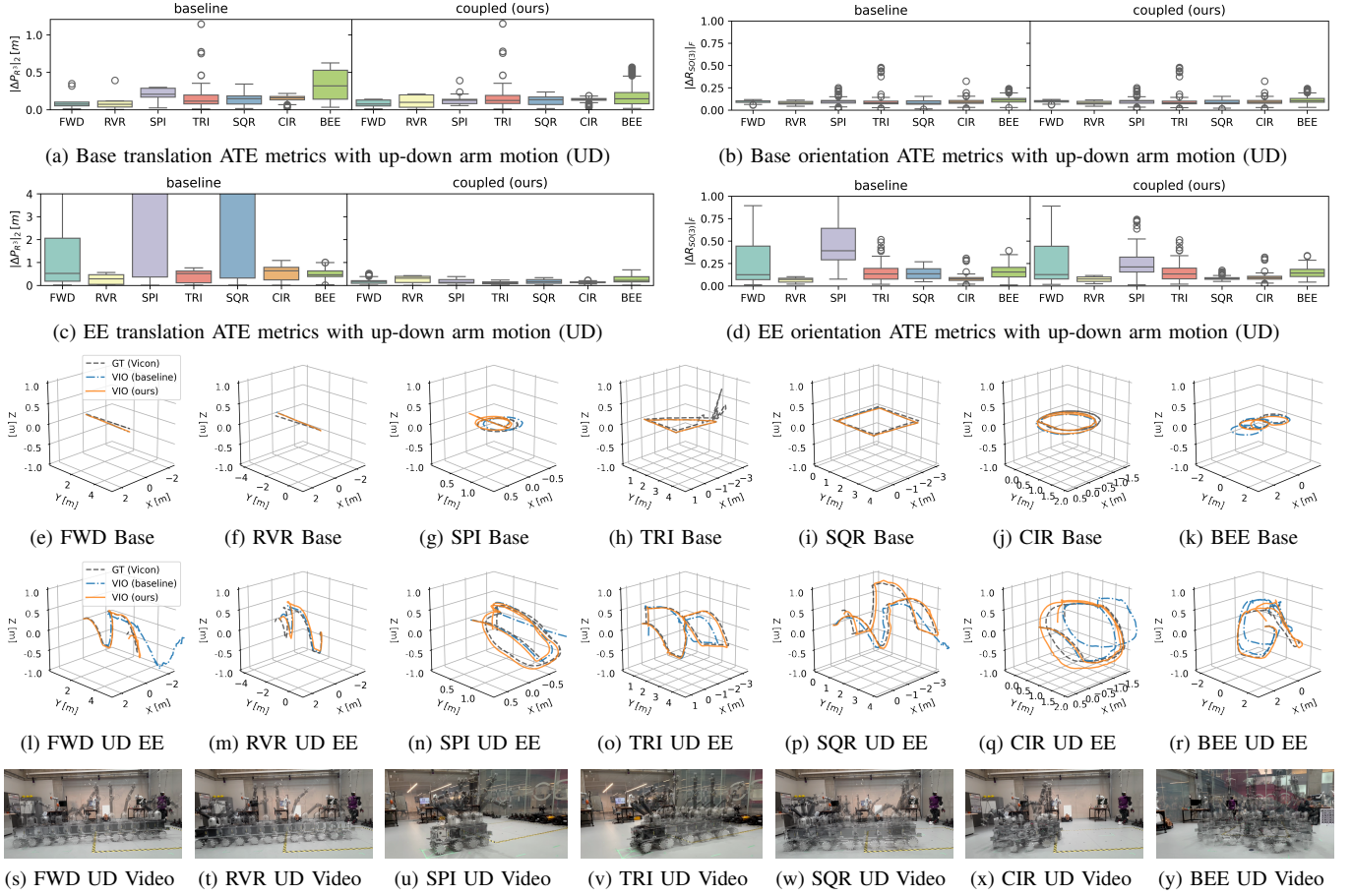


Fig. 6. A collection of box plots, 3D trajectory plots, and time-lapsed images for dual-VIO (without loop-closure) maneuvering in seven different base motions with arm sweeping up and down (UD). The box plots (a,b,c,d) demonstrate the ATE in terms of translation and orientation components for the base and EE VIO modules, respectively. The 3D trajectory plots, (e,f,g,h,i,j,k) and (l,m,n,o,p,q,r) illustrate the trajectories for the base and EE, correspondingly. There are three trajectories in each plot; the black dashed line indicates GT from Vicon, the blue dash-dotted line indicates the baseline with two VINS-Fusion in parallel, and the solid orange line showcases our proposed method with tightly-coupled dual-VIO methods through arm odometry. The seven base maneuvers at the holonomic base are indicated by time-lapse images (s,t,u,v,w,x,y), generated by super-imposing the sampled frames per 2 [s] from the recorded video.

4) *Alignment*: To ensure a fair comparison between the baseline and proposed systems, the ground truth (GT) datasets are offset absolutely after the initialization of each VIO during the algorithm's runtime. This can allow us to directly compare the VIO and corresponding GT from the initialization point.

5) *Performance Metric*: Since we are interested in VIO accuracy with dynamic locomotions, the mean of the absolute trajectory error (ATE) is employed as a performance metric. We computed ATE for translation error (e_p) and rotation error (e_q) separately so that they can provide direct insights for us to understand the overall performance of the odometry. More specifically, translation error is calculated using the l_2 norm, while rotation error is assessed by the Frobenius norm on the $SO(3)$ manifold towards identity as

$$e_p = \|\hat{\mathbf{p}}_{b_k}^w - \mathbf{p}_{b_k}^{GT}\|_2 \quad e_q = \left\| \mathbf{R}_{\hat{\mathbf{q}}_{b_k}^w}^T \mathbf{R}_{\mathbf{q}_k^{GT}} - \mathbf{I} \right\|_F \quad (8)$$

where $\mathbf{p}_{b_k}^{GT}$ and $\mathbf{R}_{\mathbf{q}_k^{GT}}$ denote the position vector and the rotation matrix, respectively, of the GT data, and $\mathbf{R}_{\hat{\mathbf{q}}_{b_k}^w}$ denotes the rotation matrix for the estimated quaternion $\hat{\mathbf{q}}_{b_k}^w$. For more details of these metrics and others, readers may refer to [51].

B. Performance Results

Among five arm motions, the up-down arm motions are the most intricate dynamic locomotion with seven different base maneuvers. In Fig. 6, the box plots 6(a) and 6(c) summarize the translation error for both the base VIO and the EE VIO. It is apparent that the translation error and its variance are significantly lower and more consistent for both VIO modules at the base and especially at the EE. However, the improvements in orientation are not as significant as shown in 6(b) and 6(d).

The rest of the locomotion (i.e. four arm motions by seven base movements) is summarized in Fig. 7 with the translational component of ATE for both VIO modules at the EE and the base. Similar to the box plots in Fig. 6, the results in Fig. 7 also suggest that our proposed method significantly improves the accuracy and consistency of the VIO at the EE, particularly when the locomotion becomes more complex. This should come as no surprise; the EE suffers from significant vibrations and excitation when the mobile base crosses the uneven terrain due to the imperfect ground levelling in the testing facility and stiff omni-wheels. By imposing the base VIO onto the EE VIO

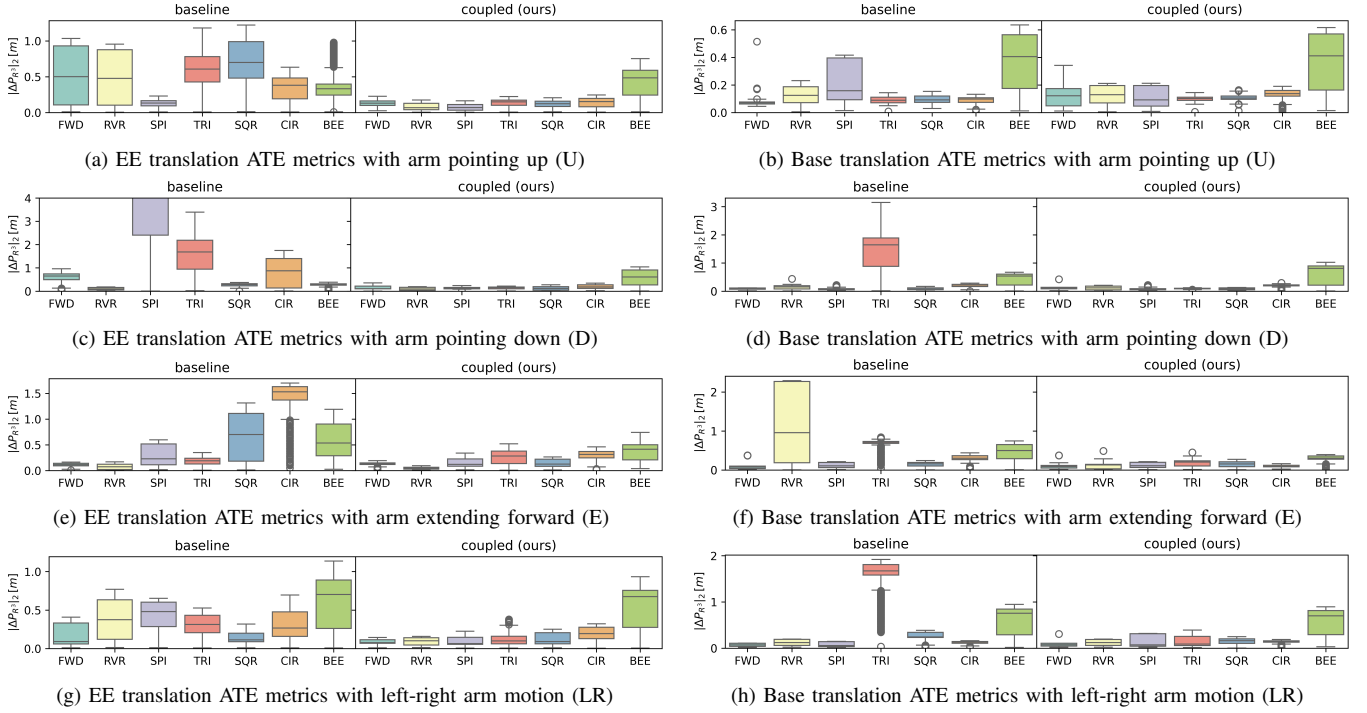


Fig. 7. A collection of box plots for dual-VIO (without loop-closure) maneuvering in all seven different base motions with four different arm motions (U, D, E, LR). The box plots (a,c,e,g) and (b,d,f,h) summarize the ATE in terms of translation components for the base and the EE VIOs, respectively.

pose graph optimization, the resultant pose estimation has been made substantially better, thereby producing robust odometry with minimal consistent ATE.

Meanwhile, performance of the base odometry appears generally similar to that of the baseline; however, it showed more consistency throughout different base motions. This is because our methods can suppress significant odometry errors from the ground impacts or visual ambiguities through the regulation of the complementary VIO estimates and thus can prevent early divergence of the VIOs upon encountering uncertainties.

As shown in Table II, the mean ATE in translation is smaller and more consistent than the baseline data (as highlighted in bold) for the dynamic locomotion involving complex base maneuvers (SPI, TRI, SQR, CIR, BEE) and active arm motions (LR, UD). The table for orientation ATE is omitted here due to page limit, but their values for our method also showed improvements over baseline results, although not as drastic as the translation ATE in Table II. (Also, see Figs. 6(b) and 6(d)).

TABLE II
MEAN ATE IN TRANSLATION AT VIOS WITH DYNAMIC LOCOMOTION

	VINS-Fusion (dual) [m]				Ours (dual+odom) [m]			
	Left-Right		Up-Down		Left-Right		Up-Down	
	EE	Base	EE	Base	EE	Base	EE	Base
FWD	0.179	0.071	1.966	0.076	0.089	0.075	0.188	0.086
RVR	0.389	0.120	0.277	0.073	0.094	0.119	0.264	0.110
SPI	0.447	0.076	4.884	0.196	0.094	0.146	0.173	0.121
TRI	0.309	1.582	0.402	0.146	0.142	0.149	0.121	0.150
SQR	0.147	0.264	45.691	0.134	0.125	0.150	0.168	0.127
CIR	0.324	0.115	0.560	0.147	0.197	0.134	0.137	0.132
BEE	0.586	0.579	0.502	0.347	0.537	0.554	0.277	0.199

Note that our method outperforms the baseline VIO not only at the EE but also at the base. Expectedly, the benefit of tight coupling between the EE VIO and the base VIO is more pronounced at the EE because the base VIO is generally more stable than the EE VIO, and thus fusing them offers major benefits to enhancing the accuracy of the EE VIO. However, the base VIO of our method also outperforms the baseline data in some cases. This is because the estimation from the EE VIO can mitigate some errors at the base VIO caused by uneven terrains and dynamic coupling with the arm motion.

V. CONCLUSIONS AND FUTURE WORK

A new tightly coupled dual-VIO scheme has been proposed for robust dual-state estimation of a mobile manipulator operating under dynamic locomotion. It moderates arm joint angles for both VIO modules (the mobile base and the EE) through arm kinematics. This fusion enables handling of degenerate modes through arbitration, thereby bringing the best out of each system; stable odometry from the base and dexterous FOV from the EE. Our approach adopts jointly optimizing two VIO modules without maintaining a single large factor graph, allowing real-time capability for multi-VIO fusion for kinematically constrained systems with aggressive dynamic locomotion. This work may be useful for active-SLAM, where the EE VIO can focus on active exploration for mapping, while the base VIO concentrates on exploitation for re-localization.

The current implementation has three major uncertainties in the arm; unobservable modes in modelling, inaccurate zeroing, and inaccurate eye-in-hand pose between the camera and the robot. These factors limit the accurate estimation of both orientation and translation for basic motions. Therefore, there

is a need for an online calibration to improve the performance further. As another future work, the proposed dual-VIO may be used in stereo mode to further improve the accuracy with the help of high bandwidth communication channel. Furthermore, we also plan to utilize mutual features between two cameras to support online temporal calibration on the fly, realizing fault tolerance and self-reinitialization capability.

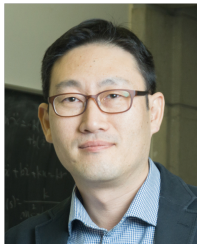
REFERENCES

- [1] C. Pu, C. Yang, J. Pu, and R. B. Fisher, "A general mobile manipulator automation framework for flexible tasks in controlled environments," *Adv. Eng. Inform.*, vol. 57, p. 102062, Aug. 2023.
- [2] I. Lluvia, E. Lazkano, and A. Ansuategi, "Active mapping and robot exploration: A survey," *Sensors*, vol. 21, no. 7, p. 2445, Apr. 2021.
- [3] W. Chen, X. Wang, S. Gao, G. Shang, C. Zhou, Z. Li, C. Xu, and K. Hu, "Overview of multi-robot collaborative SLAM from the perspective of data fusion," *Machines*, vol. 11, no. 6, p. 653, Jun. 2023.
- [4] M. Servi res, V. Renaudin, A. Dupuis, and N. Antigny, "Visual and visual-inertial SLAM: State of the art, classification, and experimental benchmarking," *J. Sens.*, vol. 2021, p. e2054828, Feb. 2021.
- [5] W. Chen, G. Shang, A. Ji, C. Zhou, X. Wang, C. Xu, Z. Li, and K. Hu, "An overview on visual SLAM: From tradition to semantic," *Remote Sens.*, vol. 14, no. 13, p. 3010, Jun. 2022.
- [6] A. I. Mourikis and S. I. Roumeliotis, "A multi-state constraint kalman filter for vision-aided inertial navigation," in *IEEE Int. Conf. on Robot. and Automat.*, Apr. 2007, pp. 3565–3572.
- [7] M. F. Ahmed, K. Masood, V. Fremont, and I. Fantoni, "Active SLAM: A review on last decade," *Sensors*, vol. 23, no. 19, p. 8097, Jan. 2023.
- [8] K. He, P. Simini, W. P. Chan, D. Kuli c, E. Croft, and A. Cosgun, "On-the-go robot-to-human handovers with a mobile manipulator," in *IEEE Int. Symp. on Rob. and Human Inter. Comm. (RO-MAN)*, Aug. 2022.
- [9] T. Sandy, L. Stadelmann, S. Kersch, and J. Buchli, "ConFusion: Sensor fusion for complex robotic systems using nonlinear optimization," *IEEE Robot. and Automat. Lett.*, vol. 4, no. 2, pp. 1093–1100, Apr. 2019.
- [10] P. M l inen, P. Mustalahti, S. Launis, and J. Mattila, "Redundancy-based visual tool center point pose estimation for long-reach manipulators," in *IEEE/ASME Int. Conf. Adv. Intell. Mechatron.*, 2020, pp. 1387–1393.
- [11] B. Ubezio, S. Sharma, G. Van Der Meer, and M. Taragna, "Kalman filter based sensor fusion for a mobile manipulator," in *Volume 5A: 43rd Mechanisms and Robot. Conf.* Amer. Soc. of Mech. Engineers, 2019.
- [12] M. Luo, E. Li, R. Guo, J. Liu, and Z. Liang, "End-effector pose estimation in complex environments using complementary enhancement and adaptive fusion of multisensor," *J. Sens.*, vol. 2021, pp. 1–18, 2021.
- [13] S. Aguilera-Marinovic, M. Torres-Torriti, and F. Auat-Che n, "General dynamic model for skid-steer mobile manipulators with wheel-ground interactions," *IEEE/ASME Trans. Mechatron.*, vol. 22, no. 1, 2017.
- [14] H.-W. Chae, J.-H. Choi, and J.-B. Song, "Robust and autonomous stereo visual-inertial navigation for non-holonomic mobile robots," *IEEE Trans. on Veh. Technol.*, vol. 69, no. 9, pp. 9613–9623, Sep. 2020.
- [15] S. Cao, X. Lu, and S. Shen, "GVINS: Tightly coupled GNSS-visual inertial fusion for smooth and consistent state estimation," *IEEE Trans. Robot.*, vol. 38, no. 4, pp. 2004–2021, Aug. 2022.
- [16] Y. Yang, P. Geneva, X. Zuo, and G. Huang, "Online self-calibration for visual-inertial navigation: Models, analysis, and degeneracy," *IEEE Trans. on Robot.*, vol. 39, no. 5, pp. 3479–3498, Oct. 2023.
- [17] T. Qin, P. Li, and S. Shen, "VINS-Mono: A robust and versatile monocular visual-inertial state estimator," *IEEE Trans. Robot.*, vol. 34, no. 4, pp. 1004–1020, Aug. 2018.
- [18] J. Vihonen, J. Honkakorpi, J. Tuominen, J. Mattila, and A. Visa, "Linear accelerometers and rate gyros for rotary joint angle estimation of heavy-duty mobile manipulators using forward kinematic modeling," *IEEE/ASME Trans. Mechatron.*, vol. 21, no. 3, pp. 1765–1774, 2016.
- [19] C. Cadena, L. Carlone, H. Carrillo, Y. Latif, D. Scaramuzza, J. Neira, I. Reid, and J. J. Leonard, "Past, present, and future of simultaneous localization and mapping: Towards the robust-perception age," *IEEE Trans. Robot.*, vol. 32, no. 6, pp. 1309–1332, Dec. 2016.
- [20] J. Jeon, S. Jung, E. Lee, D. Choi, and H. Myung, "Run your visual-inertial odometry on nvidia jetson: Benchmark tests on a micro aerial vehicle," *IEEE Robot. Autom. Lett.*, vol. 6, no. 3, pp. 5332–5339, 2021.
- [21] H. Strasdat, J. Montiel, and A. J. Davison, "Visual SLAM: Why filter?" *Image and Vis. Comput.*, vol. 30, no. 2, pp. 65–77, Feb. 2012.
- [22] Y. He, J. Zhao, Y. Guo, W. He, and K. Yuan, "PL-VIO: Tightly-coupled monocular visual-inertial odometry using point and line features," *Sensors (Basel)*, vol. 18, no. 4, p. 1159, Apr. 2018.
- [23] I. Asl Sabbaghian Hokmabadi, M. Ai, and N. El-Sheimy, "Shaped-based tightly coupled IMU/camera object-level SLAM," *Sensors*, vol. 23, no. 18, p. 7958, Jan. 2023.
- [24] Z. Song, X. Zhang, T. Li, S. Zhang, Y. Wang, and J. Yuan, "IR-VIO: Illumination-robust visual-inertial odometry based on adaptive weighting algorithm with two-layer confidence maximization," *IEEE/ASME Trans. Mechatron.*, vol. 28, no. 4, pp. 1920–1929, Aug. 2023.
- [25] S. Thrun, W. Burgard, and D. Fox, *Probabilistic Robotics*, ser. Intelligent Robotics and Autonomous Agents. Cambridge, Mass: MIT Press, 2005.
- [26] Agarwal, Sameer and Mierle, Keir and The Ceres Solver Team, "Ceres solver," Oct. 2023. [Online]. Available: <https://github.com/ceres-solver>
- [27] F. Dellaert, "Factor graphs: Exploiting structure in robotics," *Annu. Rev. Control Robot. Auton. Syst.*, vol. 4, no. 1, pp. 141–166, May 2021.
- [28] T. Zhang, Y. Tan, Z. Lei, and X. Chen, "Robust visual odometry on SE(3): Design and verification," *IEEE/ASME Trans. Mechatron.*, vol. 28, no. 4, pp. 1807–1816, Aug. 2023.
- [29] C. Zhang, Z. Yang, H. Zhuo, L. Liao, X. Yang, T. Zhu, and G. Li, "A lightweight and drift-free fusion strategy for drone autonomous and safe navigation," *Drones*, vol. 7, no. 1, p. 34, Jan. 2023.
- [30] Q. Xu, Z. Gao, C. Yang, and J. Lv, "High-accuracy positioning in GNSS-blocked areas by using the MSCKF-based SF-RTK/IMU/Camera tight integration," *Remote Sens.*, vol. 15, no. 12, p. 3005, Jun. 2023.
- [31] Y. Cao and G. Beltrame, "VIR-SLAM: Visual, inertial, and ranging SLAM for single and multi-robot systems," *Auton. Robot.*, vol. 45, no. 6, pp. 905–917, Sep. 2021.
- [32] H. Li and J. Stueckler, "Online calibration of a single-track ground vehicle dynamics model by tight fusion with visual-inertial odometry," Sep. 2023, *arXiv:2309.11148 [cs.RO]*.
- [33] Z. Zhu, Y. Kaizu, K. Furuhashi, and K. Imou, "Visual-inertial RGB-D slam with encoders for a differential wheeled robot," *IEEE Sensors J.*, vol. 22, no. 6, pp. 5360–5371, Mar. 2022.
- [34] S. Zhu, Z. Tang, M. Yang, E. Learned-Miller, and D. Kim, "Event camera-based visual odometry for dynamic motion tracking of a legged robot using adaptive time surface," May 2023, *arXiv:2305.08962*.
- [35] D. Wisth, M. Camurri, and M. Fallon, "Robust legged robot state estimation using factor graph optimization," *IEEE Robot. Autom. Lett.*, vol. 4, no. 4, pp. 4507–4514, Oct. 2019.
- [36] Y. Kim, B. Yu, E. M. Lee, J.-h. Kim, H.-w. Park, and H. Myung, "STEP: State estimator for legged robots using a preintegrated foot velocity factor," *IEEE Robot. Autom. Lett.*, vol. 7, no. 2, pp. 4456–4463, 2022.
- [37] J. Kang, H.-B. Kim, K. H. Choi, and K.-S. Kim, "External force estimation of legged robots via a factor graph framework with a disturbance observer," in *IEEE Int. Conf. on Robot. and Automat.*, 2023.
- [38] D. Wu, X. Zhong, X. Peng, H. Hu, and Q. Liu, "Multimodal information fusion for high-robustness and low-drift state estimation of UGVs in diverse scenes," *IEEE Trans. Instrum. Meas.*, vol. 71, pp. 1–15, 2022.
- [39] M. G. Mi ller *et al.*, "Robust visual-inertial state estimation with multiple odometries and efficient mapping on an MAV with ultra-wide fov stereo vision," in *IEEE/RSJ Int. Conf. on Intell. Robots and Syst.*, Oct. 2018.
- [40] L. Morra, A. Biondo, N. Poerio, and F. Lamberti, "MIXO: Mixture of experts-based visual odometry for multicamera autonomous systems," *IEEE Trans. Consumer Electron.*, vol. 69, no. 3, pp. 261–270, 2023.
- [41] C. Wang, Z. Cao, J. Li, J. Yu, and S. Wang, "Hierarchical distribution-based tightly-coupled LiDAR inertial odometry," *IEEE Trans. Intell. Veh.*, pp. 1–13, 2023.
- [42] C. Zhang, Y. Liu, F. Wang, Y. Xia, and W. Zhang, "VINS-MKF: A tightly-coupled multi-keyframe visual-inertial odometry for accurate and robust state estimation," *Sensors*, vol. 18, no. 11, p. 4036, Nov. 2018.
- [43] M. Abate *et al.*, "Multi-camera visual-inertial simultaneous localization and mapping for autonomous valet parking," Apr. 2023, *arXiv:2304.13182 [cs.RO]*.
- [44] L. Zhang, D. Wisth, M. Camurri, and M. Fallon, "Balancing the budget: Feature selection and tracking for multi-camera visual-inertial odometry," *IEEE Robot. Autom. Lett.*, vol. 7, no. 2, 2022.
- [45] Y. Alkendi, L. Seneviratne, and Y. Zweiri, "State of the art in vision-based localization techniques for autonomous navigation systems," *IEEE Access*, vol. 9, pp. 76 847–76 874, 2021.
- [46] D. Sharafutdinov *et al.*, "Comparison of modern open-source Visual SLAM approaches," *J. Intell. and Robot. Syst.*, vol. 107, no. 3, 2023.
- [47] R. M. Murray, Z. Li, and S. S. Sastry, *A Mathematical Introduction to Robotic Manipulation*, 1st ed. CRC Press, 1994.
- [48] A. Bani Younes and D. Mortari, "Derivation of all attitude error governing equations for attitude filtering and control," *Sensors*, vol. 19, no. 21, p. 4682, Oct. 2019.
- [49] "Allan variance ROS," Oxford Dynamic Robot Systems Group, Dec. 2023. [Online]. Available: https://github.com/ori-drs/allan_variance_ros

- [50] J. Rehder, J. Nikolic, T. Schneider, T. Hinzmann, and R. Siegwart, "Extending kalibr: Calibrating the extrinsics of multiple IMUs and of individual axes," in *IEEE Int. Conf. on Robot. and Automat.*, May 2016.
- [51] Z. Zhang and D. Scaramuzza, "A tutorial on quantitative trajectory evaluation for visual(-inertial) odometry," in *IEEE/RSJ Int. Conf. on Intell. Robots and Syst. (IROS)*, 2018.



Jianxiang (Jack) Xu received the B.S. degree at University of Waterloo, with distinction in Mechatronics Engineering, Honours, Co-operative Program with Artificial Intelligence Option in 2021. He is pursuing an M.Sc. degree in Mechanical and Mechatronics Engineering at the University of Waterloo and researching at the Waterloo Mechanical Systems & Control Lab. His research interests include robotics, mechatronics, system architecture, controls, state estimation, computer vision, and machine learning. He is a student member of ASME 2024.



Soo Jeon received his B.S. and M.S. degrees from Mechanical & Aerospace Engineering at Seoul National University, Korea in 1998 and 2001 respectively, and his Ph.D. from Mechanical Engineering at the University of California, Berkeley in 2007. After graduation, he worked as a mechanical engineer in Applied Materials Inc. until he moved to the Department of Mechanical & Mechatronics Engineering at the University of Waterloo in 2009, where he is currently a full professor. His research interests include dynamic systems and control, mechatronic system design, friction-induced stability and machine learning for physical systems. His research applications cover robotics, industry automation, medical ultrasound, and transportation systems. He received Rudolf Kalman Best Paper Award from ASME Dynamic Systems and Control Division (DSCD) in 2010, the Discovery Accelerator Supplement Award from NSERC (Natural Sciences and Engineering Research Council) of Canada in 2015, the Best Paper Award in Robotics at CRV (Conference on Robots and Vision) in 2022, and the Engineer of the Year Award from KOFST in 2022. He is a member of ASME, IEEE, CSME (Canadian Society for Mechanical Engineering) and PEO (Professional Engineers Ontario). He has been an associate editor for the ASME Journal of Dynamic Systems, Measurement and Control, IEEE Transactions on Automation Science and Engineering, IEEE/ASME Transactions on Mechatronics, and IEEE Robotics and Automation Letters.